

High Spatial Resolution Observations of Two Young Protostars in the R Corona Australis Region

Christopher E. Groppi¹

Steward Observatory, University of Arizona, Tucson, AZ 85721

cgroppi@as.arizona.edu

Todd R. Hunter

National Radio Astronomy Observatory, Charlottesville, VA 22903

Raymond Blundell

Smithsonian Astrophysical Observatory, Cambridge, MA 02138

Göran Sandell

SOFIA-USRA, NASA Ames Research Center, MS N211-3, Moffett Field, CA 94035

ABSTRACT

We present multi-wavelength, high spatial resolution imaging of the IRS7 region in the R Corona Australis molecular cloud. Our observations include 1.1 mm continuum and HCO^+ $J = 3 \rightarrow 2$ images from the SMA, ^{12}CO $J = 3 \rightarrow 2$ outflow maps from the DesertStar heterodyne array receiver on the HHT, 450 μm and 850 μm continuum images from SCUBA, and archival Spitzer IRAC and MIPS 24 μm images. The accurate astrometry of the IRAC images allow us to identify IRS7 with the cm source VLA 10W (IRS7A) and the X-ray source X_W . The SMA 1.1 mm image reveals two compact continuum sources which are also distinguishable at 450 μm . SMA 1 coincides with X-ray source CXOU J190156.4-365728 and VLA cm source 10E (IRS7B) and is seen in the IRAC and MIPS images. SMA 2 has no infrared counterpart but coincides with cm source VLA 9. Spectral energy distributions constructed from SMA, SCUBA and Spitzer data yield bolometric temperatures of 83 K for SMA 1 and ≤ 70 K for SMA 2. These temperatures along with the submillimeter to total luminosity ratios indicate that SMA 2 is a Class 0 protostar, while SMA 1 is a Class 0/Class I transitional object

¹NSF Astronomy and Astrophysics Postdoctoral Fellow

($L=17\pm6\ L_{\odot}$). The $^{12}\text{CO}\ J=3\rightarrow2$ outflow map shows one major and possibly several smaller outflows centered on the IRS 7 region, with masses and energetics consistent with previous work. We identify the Class 0 source SMA 2/VLA 9 as the main driver of this outflow. The complex and clumpy spatial and velocity distribution of the $\text{HCO}^+\ J=3\rightarrow2$ emission is not consistent with either bulk rotation, or any known molecular outflow activity.

Subject headings: stars: formation, ISM: individual - R CrA - Clouds - ISM: jets and outflows - ISM: kinematics and dynamics - ISM: molecules - radio lines: ISM

1. Introduction

In the past 15 years, the search for Class 0 protostellar objects has yielded only ~ 100 unambiguous sources (Froebrich 2005). Class 0 sources, which display a high ratio of submillimeter to bolometric luminosity, often remain undetectable in the near-IR, and show bolometric temperatures of 80 K or less (Myers et al. 1998). An assortment of recent observations concentrating on the core of the R Corona Australis molecular cloud (R CrA) has revealed sources that could be Class 0 objects. R CrA is an ideal laboratory for the study of low mass star formation because at a distance of ~ 170 pc, it is one of the nearest examples of this activity (Knude & Høg 1998). As a result, observations have high physical resolution (170 AU per arcsecond) when compared to more distant star forming regions. While images with the Chandra X-ray Observatory and the VLA have been able to resolve individual sources in the R CrA region, work in the (sub)millimeter band has been limited to single dish telescopes, with $> 20''$ resolution. Nevertheless, the proximity of R CrA has allowed even moderate resolution studies to reveal (sub)millimeter sources in the region that have no near-IR counterparts (Chini et al. 2003; Groppi et al. 2004a; Schöier et al. 2006).

Early single-dish observations of this region with a $2.3'$ beam identified a molecular cloud core containing the emission line star R CrA (Loren 1979). Later observations of C^{18}O with a $45''$ beam resolved this core into multiple components (Harju et al. 1993). Observing with a $23''$ beam, Henning et al. (1994) attributed the bulk of the long wavelength dust continuum emission to the deeply embedded near-IR source IRS 7 (Taylor & Storey 1984). A molecular outflow approximately centered on IRS 7 has been known for many years (Levreault 1988; Harju et al. 1993; Groppi et al. 2004a, and others), and is an indicator of protostellar activity. More recent work by Nutter et al. (2005) with the JCMT at $850\ \mu\text{m}$ and $450\ \mu\text{m}$ has begun to disentangle the submillimeter emission into numerous sources in the vicinity of IRS 7. It is now clear that IRS 7 is unlikely to be the powering source of this long wavelength dust emission. The submillimeter sources SMM1B and SMM1C (Nutter et al.

2005) are associated with two centimeter continuum point sources (Feigelson et al. 1998). These centimeter sources are also detected in the X-ray by Hamaguchi et al. (2005), with properties suggestive of Class 0 or very young Class I objects. Clearly, millimeter or sub-millimeter interferometric observations are necessary to unambiguously identify the young, embedded protostellar sources in the region.

We have observed the central region of the R CrA molecular cloud with the Submillimeter Array (SMA)¹ on Mauna Kea, Hawaii in both continuum (1.1 mm) and spectroscopic (HCO^+ $J = 3 \rightarrow 2$) mode, with the goal of spatially resolving and characterizing the Class 0 and Class I protostellar candidates in the region. In this paper, we combine the high spatial resolution SMA images with archival Spitzer IRAC and MIPS photometry, JCMT 850 μm and 450 μm maps and ^{12}CO $J = 3 \rightarrow 2$ outflow maps of moderate spatial resolution in order to more clearly reveal two young protostellar objects in the vicinity of IRS 7. Our observations range in linear resolution from 0.02 pc to 0.001 pc.

2. Observations

2.1. SMA 1.1 mm Continuum and HCO^+ $J = 3 \rightarrow 2$ Observations

R CrA IRS 7 ($\alpha_{2000.0} = 19^h 01^m 55^s.34$, $\delta_{2000.0} = -36^\circ 57' 21''.7$) was observed with the SMA on two occasions. The first track was taken on May 23, 2004 with a somewhat extended array configuration, with pads 1, 7, 8, 11, and 23 used. The zenith opacity at 225 GHz as measured with the tipping radiometer at the Caltech Submillimeter Observatory (CSO) ranged from 0.14 to 0.20 during the observations. The tuning was chosen to place the HCO^+ $J = 3 \rightarrow 2$ line (267.557619 GHz) in correlator chunk 3 of the lower sideband with $v_{\text{LSR}} = +6$ km s^{-1} (corresponding to a local oscillator setting of 271.77 GHz). The spectral resolution was 256 channels per correlator chunk (0.312 MHz, or 0.35 km s^{-1} per channel). Uranus and Neptune were observed for bandpass and flux calibration, while the quasar J1924-292 (5.5 Jy) was used as the primary gain calibrator and pointing source. The UV data span 8 to 100 $k\lambda$, with the greatest coverage between ~ 20 and 60 $k\lambda$. The primary beamsize was $46''$. The second track of data was taken on October 4, 2004 in the compact-north configuration, with antennas on pads 1, 5, 7, 8, 9, 10, 12 and 16. Seven of the eight antennas provided usable data for this track. These data were taken in a hybrid resolution mode with 512 channels per chunk (0.156 MHz, 0.18 km s^{-1}) for the HCO^+ $J = 3 \rightarrow 2$ correlator chunk, and 128

¹The Submillimeter Array (SMA) is a collaborative project between the Smithsonian Astrophysical Observatory and the Academia Sinica Institute of Astronomy & Astrophysics of Taiwan.

channels (0.625 MHz, 0.70 km s^{-1}) for all other chunks. In an attempt to detect the source SMM 1A, a second source position was observed one half of a primary beam south of IRS 7. The calibration sources and observing strategies were otherwise identical to the first track.

These data were calibrated and reduced with the MIRIAD software package with extensions for the SMA using the procedures outlined in Zhao (2006). The continuum data were constructed using all the line-free “chunks” of the correlator to produce images for the north and south pointings. The south pointing was not added into the final image, because no source was detected. The continuum data were inverted to the image domain using uniform weighting, then cleaned using a gain of 0.08 with 2500 iterations. An rms noise of 9 mJy/beam was achieved. The synthesized beam is $4''.2 \times 1''.7$ ($700 \times 300 \text{ AU}$) with a position angle (p.a.) of 27° . We estimate the absolute astrometric uncertainty to be $0''.3$ and the flux scale uncertainty to be 20%. The spectrometer “chunk” with the $\text{HCO}^+ \text{ J} = 3 \rightarrow 2$ line was extracted from the data of the two tracks and independently processed. The data from the second track were binned to match the spectral resolution of the first track prior to processing. The data were then calibrated and reduced in a similar fashion to the continuum data. Inversion to the image domain was performed with natural weighting for maximum sensitivity. Cleaning was performed with a gain of 0.08 and 2500 iterations. As with the continuum, no line emission was detected in the southern pointing.

2.2. Heinrich Hertz Telescope $^{12}\text{CO J} = 3 \rightarrow 2$ Observations

The $^{12}\text{CO J} = 3 \rightarrow 2$ data for this work was taken with the 10 m Heinrich Hertz Telescope at Mt. Graham, AZ during April, 2006 with the DesertStar 7 beam heterodyne array receiver (Groppi et al. 2004b). $5' \times 5'$ maps centered on IRS 7 were taken in the on-the-fly (OTF) observing mode, using the facility 1 MHz resolution filter bank spectrometers. Eight OTF maps were made over the course of the run, and later coadded. The spectral resolution is 0.87 km s^{-1} , with a spatial resolution of $23''$. Hot-sky calibrations were done once per row, with cold load calibrations done once per map. Data were gridded and combined based on RMS weighting using the CLASS software package. The intensities of each pixel were scaled using their measured main beam efficiency before combining. Further analysis was performed using the IDL package.

2.3. James Clerk Maxwell Telescope 850 μm and 450 μm Observations

The 850 μm and 450 μm continuum observations were obtained with bolometer array SCUBA on JCMT², Mauna Kea, Hawaii. SCUBA (Holland et al. 1999) has 37 bolometers in the long and 91 in the short wavelength array separated by approximately two beam widths in a hexagonal pattern. The field of view of both arrays is $\sim 2'3$. Both arrays can be used simultaneously by means of a dichroic beamsplitter.

The SCUBA observations reported in this paper were all obtained in jiggle-map mode (Holland et al. 1999) with chop throws of $120''$ - $150''$ in azimuth. Because the R CrA cloud complex is rather extended, it was impossible to completely chop off the array, but any strong emission in the off source positions was carefully blanked out in the data reduction stage and should not affect the morphology or photometry of the point-like sources in the field. It does, however, affect the integrated flux density of the extended cloud emission, which is irrelevant for our analysis, since we are only interested in the embedded compact sources in the cloud.

The data used in this paper come from three 5-integration maps obtained during SCUBA commissioning on March 30 and April 5, 1997. These maps were obtained in excellent submillimeter conditions with CSO $\tau_{225\text{GHz}} \sim 0.045$ - 0.05 . Analysis of this data set was discussed by van den Ancker (1999). We additionally searched the JCMT archive at the CADC³ and found one more 6-integration map⁴ obtained in good submillimeter conditions (CSO $\tau_{225\text{GHz}} \sim 0.066$) on April 11, 2000, which we added to our data set. Pointing corrections were derived from observations of the blazar 1929-293 and flux calibration from observations of Uranus. We estimate the calibration accuracy to be better than 10% at 850 μm and better than 20% at 450 μm . The measured Half Power Beam Width (HPBW) for the 1997 and 2000 observations are remarkably similar. In 1997 we used a $120''$ chop throw, but an experimental chop waveform, which broadened the beam in the chop direction, while the observation from April 2000 used a $150''$ chop throw, which also broadened the beam by about the same amount. The HPBW is therefore $\sim 15''.6 \times 13''.5$ and $9''.1 \times 7''.8$ for 850 μm and 450 μm , respectively with the major axis aligned with the chop direction.

²The JCMT is operated by the Joint Astronomy Centre, on behalf of the UK Particle Physics and Astronomy Research Council, the Netherlands Organization for Scientific Research, and the Canadian National Research Council.

³Guest User, Canadian Astronomy Data Center, which is operated by the Dominion Astrophysical Observatory for the National Research Council of Canada's Herzberg Institute of Astrophysics

⁴This map is from the data set published by Nutter et al. (2005)

The data were reduced in a standard way using SURF (Jenness and Lightfoot 1999; Sandell, Jessop and Jenness 2001) and STARLINK imaging software, i.e., we flat fielded, extinction corrected, sky subtracted, despiked, and calibrated the images in Jy beam⁻¹. We then pointing corrected each data set for any drift in pointing between each pointing observation and added the data together to determine the most likely submillimeter position at 850 μ m. Once we had derived a basic 850 μ m astrometric image, we made Gaussian fits of point-like sources for each data set and derived small additional RA and Dec corrections to each scan (shift and add) to sharpen the final image to this position. Manual Gaussian fitting for these closely spaced, embedded sources is more reliable than automatic clump finding routines (e.g. clumpfind), which often do not find clumps embedded in an extended cloud, especially if those clumps are close to each other. Since there is a small mis-alignment between the 850 and 450 μ m arrays, we first corrected the 450 μ m images for any pointing drifts and then did shift and add using an isolated compact source in the 850 μ m image as an astrometric reference source for the 450 μ m data. We estimate the astrometric accuracy in our SCUBA images to be $\leq 2''$.

The final coadd was done by noise-weighting the data in order to minimize the noise in the final images. The images were coadded by weighting with the inverse square of the noise in each set and accounting for the difference in integration time. The first image is taken as a reference and then the weighting factors are computed for each subsequent image:

$$w_2 = \left(\frac{t_2/t_1}{\sigma_2/\sigma_1} \right)^2 \quad (1)$$

This method minimizes the noise in the final coadded image. The rms of the 450 μ m image is ~ 0.3 Jy beam⁻¹ and ~ 12 mJy beam⁻¹ for the 850 μ m image. All our maps were converted to FITS-files and exported to MIRIAD (Sault, Teuben and Wright 1995) for further analysis. In order to correct for the error lobe contribution, especially at 450 μ m, we have deconvolved all the maps using CLEAN and an elliptical model beam derived from our Uranus observations. Our model beam is composed of three symmetric Gaussians: a main beam, a near-error lobe, and an extended, low amplitude, far-error lobe. We rotated this model beam to the approximate rotation angle of each individual map and took the average of the rotated beams to provide a more accurate model beam for our coadded maps.

3. Analysis

3.1. SMA continuum results

Figure 1 shows the SMA 1.1 mm continuum image. We detect two sources of approximately equal flux density. The positions and flux densities derived from two-dimensional Gaussian fits to the sources are given in Table 1. SMA 1, the eastern source, is marginally resolved, with an estimated source size of $1''.1 \times 0''.5$ at p.a. = 58° . The western source, SMA 2, is unresolved. SMA 1 coincides to within $0''.16$ of a centimeter source designated by various names: VLA 10E (IRS 7B) by Brown (1987), source 8 (Feigelson et al. 1998), and source 14/IRS7E (Forbrich et al. 2006, 2007). SMA 1 also coincides within $0''.17$ of the hard X-ray source CXOU J190156.4-365728 (Hamaguchi et al. 2005). SMA 1 is detected in all IRAC bands and at $24\ \mu\text{m}$ with MIPS (see Section 3.3 and Table 3). In contrast, SMA 2 is not seen in either the X-ray, near-IR or mid-IR bands, but its position is consistent with a centimeter source designated by various names: source 9 by Brown (1987), source 6 by Feigelson et al. (1998), and source 11 by Forbrich et al. (2006). The SMA position of SMA 2 is within $0''.5$ of the S-band position reported by Brown (1987) which agrees to $0''.1$ of the X-band contour map peak of Forbrich et al. (2006). Although those authors do not quote position uncertainties, Feigelson et al. (1998) notes that the VLA position accuracy for their data on this low declination (i.e. very low elevation) source is $\pm 1''$. Even if the VLA position is accurate to $\pm 0.2''$, this uncertainty combined with the SMA position uncertainty allow for the possibility that the 1.1 mm emission from SMA 2 is coincident with the centimeter source. SMA 2 also is within $0''.93$ of the 7 mm VLA source CT2 (Choi & Tatematsu 2004); the implications of this possible association are discussed later. SMA 1 and SMA 2 coincide with the two sub-mm sources SMM 1B and SMM 1C Nutter et al. (2005), which is seen more clearly in our SCUBA data (Section 3.2). We do not detect IRS 7A (VLA 10W, Feigelson 7, Forbrich 12/IRS7W), nor do we detect any sources in the “prestellar” core SMM 1A, which is the brightest extended source in the submillimeter continuum, located $\sim 20''$ south of IRS 7.

3.2. SCUBA $450\ \mu\text{m}$ and $850\ \mu\text{m}$ results

Our $850\ \mu\text{m}$ and $450\ \mu\text{m}$ SCUBA images (Figure 2) agree qualitatively with the SCUBA results of Nutter et al. (2005), although we have better signal-to-noise and image quality due to a larger data set and improved data processing methods. We detect all the sub-mm sources seen by Nutter et al. (2005) and additionally we identify a fainter core south of SMM 1A. Although SMM 1A is not resolved at $850\ \mu\text{m}$, the $450\ \mu\text{m}$ image suggests that it consists of two cores, rather than a single elongated elliptical core. This was also seen

by van den Ancker (1999) in a high spatial resolution 800 μm -map and van den Ancker therefore listed SMM 1A as two separate sources. We have used the MIRIAD task IMFIT to fit elliptical Gaussians with a two-component Gaussian fit; one compact component for the core and an extended Gaussian for the surrounding cloud. Even though the surrounding cloud may not be well described by a single Gaussian, this approach works reasonably well if one limits the region over which the fitting is done, so that the extended cloud emission can be approximated by a single Gaussian. For very extended cores like SMM 1A and SMM 4 we approximated the surrounding cloud emission with a baseline plane rather than a Gaussian. The uncertainty in the estimation of the background, however, adds about a 10 - 15% error to the integrated flux densities. The integrated flux densities and positions for the submillimeter continuum sources are given in Table 2. These flux densities differ significantly from the flux densities quoted by Nutter et al. (2005), because their results include emission from the surrounding cloud.

Only two of the known near-IR sources (IRS 1 and WBM 55) in the R CrA cloud core coincide with compact submillimeter SCUBA sources, but in our high spatial resolution 450 μm image we also resolve the two 1.1mm SMA continuum sources, SMA 1, and SMA 2 as two separate compact dust emission peaks. IRS 5 and the new mid-IR source IRAC 9 (Table 3) lie close to the peak of the extended submillimeter core SMM 4, but we see no detectable dust emission excess from the stars themselves, even though our ^{12}CO $J = 3 \rightarrow 2$ observations (Section 3.4) indicate that there may be a molecular outflow powered by one of these stars. Neither do we detect dust emission from the two young HAEBE stars R CrA and T CrA. R CrA is the most luminous source in the region (Wilking, Taylor & Storey 1986). It is very strong in the mid-IR and illuminates a large reflection nebula. It is possible that the star may still be associated with a compact dust disk, but since it is situated near the cloud ridge encompassing SMA 1 and 2 (Figure 2), it is difficult to detect it, especially if the disk is small. From our 450 μm image we estimate that the emission from such a disk would be less than 0.7 Jy beam^{-1} . Using the dust grain formalism of Hildebrand (1983), this flux density limit corresponds to a mass limit of $< 1.2 \times 10^{-2} M_{\odot}$ (assuming $T = 30K$ and $\beta = 1$, i.e. the average disk SED parameters found in the survey of Andrews & Williams (2005)).

IRS 1, also known as HH 100-IR, illuminates a prominent cigar-shaped reflection nebula (Hartigan & Graham 1987; Graham 1993) with an HH object (HH 97) near the tip of the nebula, indicating that one sees the cavity walls of an outflow driven by IRS 1. WBM 55 is near the HH objects HH 104 A & B, but these are probably excited by SMA 2 (see Section 3.4) or some other young star in the vicinity of SMA 2. Nevertheless it is likely that WBM 55 also drives an outflow. However, we do not see any dust emission from IRS 7, which has been suggested as a possible candidate for driving the large scale CO outflow (Levreault 1988; Groppi et al. 2004a; Wilking et al. 1997). IRS 7 is deeply embedded ($A_V >$

35^m) in the cloud core and appears as a nebulous knot in K band. Wilking et al. (1997) suggested that the $2.2\ \mu\text{m}$ emission may originate from the nebulosity and that the star itself is invisible at K band. This suggestion gets further support from the high contrast images presented by Chen & Graham (1993) and Hamaguchi et al. (2005) which show a larger reflection nebulosity to the northeast seemingly forming a bipolar nebula. In this scenario one would expect the mid-IR (i.e. IRAC emission) and VLA radio source to pinpoint the location of the star and place it northwest of the near-IR position. Hamaguchi et al. (2005) derive an accurate $2.2\ \mu\text{m}$ position, which is slightly north of the IRAC/VLA position, suggesting that the $2.2\ \mu\text{m}$ emission has the same energy origin as the mid-IR emission. To illustrate the complexity of this region we display a sub-image of the $450\ \mu\text{m}$ image covering only SMA 1, IRS 7 and SMA 2 in Figure 3. Here we overlay the IRAC positions (Table 3), the cm VLA positions from Feigelson et al. (1998), and the 7 mm VLA positions from Choi & Tatematsu (2004). This figure shows clearly that SMA 2 and IRS 7 are different objects.

3.3. Spitzer IRAC and MIPS archival data

We retrieved Spitzer GTO observations for the R CrA region from the Spitzer data archive (Megeath et al. 2004). These GTO observations included IRAC images at $3.6\ \mu\text{m}$, $4.5\ \mu\text{m}$, $5.8\ \mu\text{m}$, and $8.0\ \mu\text{m}$, as well as MIPS observations at $24\ \mu\text{m}$ ⁵. Figure 4 shows a composite IRAC $4.5\ \mu\text{m}$ image derived from the “long” and “short” exposure time images for increased dynamic range. The spatial resolution of IRAC permitted the use of simple aperture photometry using the Starlink Gaia package to extract positions and flux densities for all 8 μm sources within a $2'$ radius of IRS 7 (Table 3). The photometric uncertainty is estimated at $\sim 10\%$, dominated by the uncertainty of the background level in the artifact-filled field. The astrometric accuracy of the IRAC images ($\leq 0''.3$) confirms that the infrared object IRS 7 is associated with the VLA source IRS 7A (VLA 10W) (Brown 1987; Feigelson et al. 1998) and the hard X-ray source X_W (Hamaguchi et al. 2005). For the first time we also detect an infrared counterpart to the radio source IRS 7B (VLA 10E), which we have identified as SMA 1 in our 1.1 mm continuum imaging. We have also discovered a new, relatively faint mid-IR source, IRAC 9, $\sim 9''$ northeast of IRS 5.

The pipeline reduced “Post-BCD” MIPS images were used to obtain aperture and PSF fitted photometry for any $24\ \mu\text{m}$ sources in the vicinity of SMA 1 and SMA 2. SMA 1 was

⁵The spatial resolution of the 70 and $160\ \mu\text{m}$ MIPS data were too coarse to reveal any source information in the R CrA cloud core.

clearly detected at $24\ \mu\text{m}$ but it was saturated and very near the sources IRS 7 and R CrA, which were also badly saturated. We estimated flux densities by fitting the unsaturated wings of the PSFs to create a “restored” unsaturated PSF for flux estimation. The process was iterative. We first fit R CrA (200 ± 20 Jy), and subtracted the model PSF from the image, then fit IRS 7 (65 ± 15 Jy), and finally fit SMA 1 (20 ± 5 Jy). The flux density obtained by this procedure agrees quite well with ground based photometry. Wilking, Taylor & Storey (1986) quote 218 ± 6 Jy for R CrA and 37 Jy for IRS 7 at Q ($20\ \mu\text{m}$). After the subtraction of the three model PSFs, there was no indication that SMA 2 was detected. The fitting and subtraction of the highly saturated PSFs likely masked any faint emission from SMA 2. We use the flux density uncertainty estimate of SMA 1 to place an upper limit on the flux density of SMA 2 ≤ 5 Jy.

3.4. CO outflows

We have constructed outflow maps from $^{12}\text{CO}\ J = 3 \rightarrow 2$ HHT data which provide moderate ($23''$) spatial resolution. Figure 5 shows the CO outflow red and blue contours. The velocity intervals used to produce the red and blue contours are similar to Groppi et al. (2004a), at -10 to $+3\ \text{km s}^{-1}$ for the blue wing, and 10 to $21\ \text{km s}^{-1}$ for the red wing. These data provide about three times the spatial resolution of Groppi et al. (2004a), and confirm that the center of the outflow is in the vicinity of IRS 7. Even with this spatial resolution the CO map gives the appearance that the high velocity emission is dominated by a single outflow centered near IRS 7 and SMA 2. A closer inspection, however, shows features which are hard to explain with a single outflow. This is not surprising, since we know that there is a young cluster embedded in the molecular cloud core, several of which appear to be surrounded by active accretion disks. We plot the optically-detected emission line objects (HH objects) from Graham (1993) and Wang et al. (2004) in figure 5. In figure 5 we draw a line connecting the peaks of the red and blue outflow lobes. This line (at p.a. 105°) passes almost exactly through SMA 2, and also is very close to the HH104 objects. Wang et al. (2004) believe that HH104 C and D are associated with IRS6 and a nearby optically detected jet, and not associated with HH104 A and B. The spatial association of HH104 C and D with the SMA 2 outflow axis could therefore be coincidental. SMA 2 is also located at the approximate EW center of the CO outflow lobes. We believe this is sufficient evidence to attribute the major outflow activity in the region to SMA 2. Further evidence for this conclusion comes from the fact that in all 13 of the molecular lines measured by Schöier et al. (2006), the FWHM linewidths are broader when the APEX telescope beam encompasses SMA 2, compared to SMA 1.

We also find a second, smaller CO outflow, centered on the infrared source HH100-IR (Strom et al. 1974), with the outflow axis parallel to the line connecting the HH objects HH 98 (slightly red-shifted) and the two blue-shifted HH-objects HH 100 and HH 97. This outflow could also be associated with HH99A and HH99B (Cohen et al. 1984). A measured proper motion for HH99 reported by Caratti o Garatti et al. (2006) is at a similar position angle to the line connecting the outflow lobes shown in 5. The blue-shifted outflow lobe is less prominent than the optical/near-IR cavity, presumably because the blue outflow emerges out of the dense cloud core into the low density halo, and therefore encounters much less gas to interact with. Other small outflows could exist, but do not have the reinforcing evidence of the presence of optically-detected emission line objects. SMA 1, for example, could be driving an outflow oriented NNW, which could explain the blue-shifted ridge northwest of SMA 2, although there is also faint blue-shifted emission to the south of SMA 1. Another possibility for the blue-shifted ridge NW of SMA 2 is a roughly E-W outflow from IRS 6. Alternatively, the red-shifted emission in the vicinity of IRS 6 could be part of a NE-oriented red-shifted outflow lobe originating from or near IRS 5 with the blue outflow lobe too faint to be detected in the low-density cloud SW of IRS 5. One will need much higher spatial resolution and sensitivity to disentangle the outflows from the young stars in the R CrA core. Therefore, in the following analysis, we compute mass estimates from the integrated red-shifted and blue-shifted emission as if it originates from a single outflow. We assume that the excitation temperature is equal to the peak CO line temperature at each map position (i.e. the line cores are optically thick), and the line wings are optically thin. We compute the total mass and energetics for the entire outflow complex. Following Snell et al. (1984),

$$N_{CO} = \frac{1.94 \times 10^3 f^2}{A_{ul}} \frac{kT_{ex}}{hB_0g_u} \int T_R(CO) dV \exp\left(-\frac{E_{uk}}{T_{ex}}\right) cm^{-2} \quad (2)$$

We calculate a red lobe mass of $0.04 M_{\odot}$, and a blue lobe mass of $0.03 M_{\odot}$, assuming a CO abundance relative to H_2 of 1.5×10^{-4} (Hogerheijde 2003). This is considerably less than the masses calculated for the outflow in Groppi et al. (2004a), but these data cover only a quarter of the area on the sky. In addition, the assumption that the line wings are optically thin make these estimates lower limits for the mass. As shown for $^{12}\text{CO } J = 1 \rightarrow 0$ in Groppi et al. (2004a), this assumption leads to an underestimation of the mass in the outflow by a factor of several, depending on the level of self absorption in the line. Also, the filling factor of the warmer gas traced by $^{12}\text{CO } J = 3 \rightarrow 2$ could be less than in the case of $^{12}\text{CO } J = 1 \rightarrow 0$. With these caveats, the mass and associated momentum, kinetic energy and mechanical luminosity are consistent with the results found in Groppi et al. (2004a).

3.5. Interferometric $\text{HCO}^+ \text{ J} = 3 \rightarrow 2$ Observations

The interferometric $\text{HCO}^+ \text{ J} = 3 \rightarrow 2$ observations reveal a very clumpy distribution of emitting gas with a complex velocity field. Clearly, the lack of short spacing information severely limits the contents and fidelity of the image. Lines are typically about 2 km s^{-1} wide, and can exhibit complex line shapes. A simplified contour plot with “red” and “blue” contours is shown in Figure 6. This plot shows that the clumps of $\text{HCO}^+ \text{ J} = 3 \rightarrow 2$ emission seem to follow a roughly spherical distribution around SMA 2, and show no systematic spatial distribution of velocity. In addition, the $\text{HCO}^+ \text{ J} = 3 \rightarrow 2$ clumps are not spatially coincident with either of the continuum sources SMA 1 or SMA 2. The velocities of the clumps are also not consistent with the velocity distribution of the molecular outflow seen in $^{12}\text{CO} \text{ J} = 3 \rightarrow 2$. The observed clumpy, chaotic velocity field also does not support the hypothesis of a circumstellar or circumbinary disk, as was suggested based on the kinematics of single-dish observations of $\text{HCO}^+ \text{ J} = 4 \rightarrow 3$ (Groppi et al. 2004a).

This clumpy structure might be the result of the interaction of many outflows from the large number of protostars in the region. The velocity field of the clumps does not seem to correlate with the large scale outflows seen in $\text{CO} \text{ J} = 3 \rightarrow 2$, but the complexity of the region is high, and the interferometric image obviously suffers from missing flux. Another explanation for the observed morphology is that the clumps are knots in a spherical shell of material swept-up by the molecular outflows and winds produced by the young cluster. The critical density of the $\text{HCO}^+ \text{ J} = 3 \rightarrow 2$ transition in which the clumps are observed suggests the density is of the order $\sim 10^7 \text{ cm}^{-3}$. In addition, the spatial filtering provided by the interferometer also favors the detection of clumpy structure. If this is the case, we can calculate an upper limit on the mass of the possible gaseous shell by assuming the gas is distributed in a uniform sphere, and that the column density is that of the brightest clump. Assuming the lines are optically thin, we can calculate the column density in the same manner as the previous section. We can then estimate the mass by integrating over a circle of diameter $45''$ ($8.5 \times 10^{16} \text{ cm}$ at a distance of 170 pc). We convert the flux density to brightness temperature using the following formula:

$$T_B(K) = \frac{0.048 \nu(\text{GHz})}{\ln\left(1 + \frac{3.92 \times 10^{-8} \nu(\text{GHz})^3 \theta_1 \theta_2}{F_\nu(\text{Jy})}\right)} \quad (3)$$

where θ_1 and θ_2 are the FWHM dimensions of the source region (in this case, the beam size). This results in a $\text{HCO}^+ \text{ J} = 3 \rightarrow 2$ brightness temperature of 17.7 K , and an integrated intensity of 24.3 K km s^{-1} . Assuming an abundance of HCO^+ to H_2 of 1.2×10^{-8} (Hogerheijde 2003), we calculate a shell mass of $2.1 \times 10^{31} \text{ g}$, or 0.01 M_\odot . With an expansion velocity of

$\sim 1.5 \text{ km s}^{-1}$, the momentum and kinetic energy of the shell is small compared to that of the large scale molecular outflow. Thus, the driving source(s) of the outflow(s) are easily capable of driving the expansion of such a shell, although the mechanism is unclear. Alternatively, the shell could be driven by a wind from a more evolved pre-main-sequence star like IRS 7.

It is important to note that the ring like morphology we see in the interferometric HCO^+ map could be the result of a lack of zero spacing and short spacing data, rather than a reflection of the true gas morphology. Future observations with combined interferometric and single dish data will be necessary to generate an unambiguous determination of the gas morphology around SMA 2.

4. Discussion

4.1. FIR Spectral Energy Distributions

The SMA 1.1mm data and SCUBA 850 μm and 450 μm data are combined with the MIPS and IRAC archival data to produce SEDs capable of constraining the peak of a greybody, thereby estimating the source temperature. The source SEDs and greybody fits are shown in Figures 7 and 8. Neither source is detected in the near-infrared. The upper limits plotted are from Wilking et al. (1997) who quote 3σ upper limits of (17.5, 17.0 16.5) for the (J , H , K) bands. We fit SMA 1 with a two-temperature composite greybody. The uncertainties in the fitted and derived parameters have been estimated by perturbing the flux densities by 1σ (in such a way as to maximize the change in fitted temperature) and repeating the fit. We find temperatures of $55 \pm 3 \text{ K}$ and $344 \pm 6 \text{ K}$ for the two components, with a low frequency dust grain emissivity index $\beta = 1.3 \pm 0.2$. The warmer greybody was assumed to have $\beta = 1.0$. The integrated bolometric luminosity based on the SED for SMA 1 is $17 \pm 6 \text{ L}_\odot$. The total mass is $(3.5 \pm 1.4) \times 10^{-2} \text{ M}_\odot$, assuming a gas to dust mass ratio of 100. The ratio of submillimeter luminosity to total luminosity in SMA 1 is $(1.4 \pm 0.4) \times 10^{-3}$, suggestive of a class 0/I source. The near infrared flux density upper limits are a factor of 2.5×10^6 less than the SED peak ($\approx 260 \text{ Jy}$ at $62\mu\text{m}$), suggestive of a Class 0 source (Froebrich 2005). We also calculate the bolometric temperature of the source following Myers & Ladd (1993). The bolometric temperature T_{bol} of a SED F_ν is defined as the temperature of a blackbody having the same mean frequency $\bar{\nu}$:

$$T_{bol} \equiv [\zeta(4)/4\zeta(5)]h\bar{\nu}/k = 1.25 \times 10^{-11} \bar{\nu} \text{ K Hz}^{-1}, \quad (4)$$

where $\zeta(n)$ is the Riemann zeta function of argument n , h is Planck's constant, k is Boltzmann's constant, and the mean frequency $\bar{\nu}$ is the ratio of the first and zeroeth frequency

moments of the spectrum:

$$\bar{\nu} \equiv I_1/I_0, \quad I_m \equiv \int_0^\infty d\nu \nu^m F_\nu. \quad (5)$$

We numerically integrate the fitted SED to obtain a bolometric temperature of 83 K for SMA 1.

For SMA 2, only an upper limit exists for the 24 μm flux density, so we have determined the maximum and minimum temperature greybodies consistent with this mid-infrared upper limit and the 1.1 mm and submm detections. We find a maximum temperature of 63 K, and a long wavelength dust emissivity index of $\beta = 0.6$. The maximum luminosity is then $\leq 3.3 L_\odot$, the mass is $6.4 \times 10^{-3} M_\odot$, and the bolometric temperature is ≤ 70 K. The lower limit to the source temperature is 23 K, with a dust emissivity index of $\beta = 0.8$. This corresponds to a minimum luminosity of $0.15 L_\odot$, and a mass of $4.5 \times 10^{-2} M_\odot$. The ratio of submillimeter luminosity to total luminosity in SMA 2 is between 3.4×10^{-3} (cold limit) and 6.6×10^{-2} (warm limit). The near-infrared flux density upper limits are between 2.5×10^4 (cold limit) and 3.3×10^5 (warm limit) times less than the SED peak. Both of these ratios are consistent with typical characteristics of a Class 0 source (Froebrich 2005).

Considering the 7 mm data of Choi & Tatematsu (2004), we note that our SED predicts 1.9 mJy from SMA 2 at that wavelength, whereas the measured value is 2.4 ± 0.7 mJy. We also note that the positions agree to within $0''.9$, with most of the offset in declination. Considering the low-elevation of the source when observed at the VLA, the offset could be due to instrumental uncertainty. These facts leads us to favor the interpretation that much of the emission from CT2 is dust emission from SMA 2. A lesser portion of the 7 mm flux density ($\sim 0.5 - 1$ mJy) could be due to free-free emission from an ionized jet as it would still be consistent with a relatively flat centimeter-wave spectral index (e.g. Reynolds (1986)).

4.2. Non-detections of other 7mm sources

In addition to CT2, Choi & Tatematsu (2004) detected four more point sources in the IRS 7 field at 7 mm with the VLA which we do not detect with the SMA. CT4 has a negative spectral index, $\alpha \sim -0.8 \pm 0.1$, i.e. the emission appears non-thermal, possibly gyrosynchrotron emission, although Feigelson et al. (1998) did not detect any polarized emission. However, inspection of the data by Brown (1987) and Feigelson et al. (1998) suggest that the centimeter VLA emission is variable; it could therefore still be free-free emission if the source was in a low state at the time of the 7 mm observations. Due to their non-detection at cm wavelengths, CT 1, CT 3, and CT 5 were hypothesized to have steep spectra ($\alpha \geq 2.3$). With no IR counterparts, Choi & Tatematsu (2004) suggest that the emission originates in

compact dust disks around young low-mass stars. CT 1 could be associated with a faint $450\ \mu\text{m}$ peak seen to the northeast of SMA 2 (Figure 3), but we definitely see no $450\ \mu\text{m}$ excess from CT 5. Furthermore, the SMA should have detected these objects easily if they have temperatures typical of dust disks (20-30K). If the 7mm emission from these objects is from dust, the only way their SEDs can be consistent with the SMA non-detections and the VLA 3.6cm non-detections is if they are very cold ($T \sim 6\text{K}$) and remain optically thick ($\tau > 1$) at wavelengths shortward of 1 cm. In this scenario, they could represent compact accretion cores just prior to the formation of a stellar embryo, such as the 10K “Class -1” objects predicted by Boss & Yorke (1995). In any case, the reality and nature of these potentially interesting objects warrant further observations with ATCA or eVLA.

4.3. Are SMA 1 and SMA 2 Class 0 Protostars?

Both Nutter et al. (2005) and Schöier et al. (2006) postulate that either one or both of the young stellar objects which we associate with SMA 1 and SMA 2 are Class 0 protostars. Forbrich et al. (2006) and Forbrich et al. (2007) suggest that SMA 1 is a candidate Class 0 source, but do not detect SMA 2 in their VLA and Chandra observations. Our data suggest that SMA 2 is a Class 0 source, while SMA 1 straddles Class 0 and Class I. It is clear that both SMA 1 and SMA 2 are submillimeter bright objects with centimeter radio counterparts, hard X-ray counterparts, and no detected near-IR counterparts. We see no evidence for binary association. Neither object is detected at near-infrared wavelengths, but SMA 2 is detected in all four IRAC bands. At $24\ \mu\text{m}$ we detect SMA 1 and can only place an upper limit on the flux of SMA 2, but the proximity to two extremely bright sources (R CrA and IRS 7) have likely masked any $24\ \mu\text{m}$ flux that may originate from SMA 2. With a bolometric temperature upper limit of 70 K, no IRAC or near-IR detections, and the presence of a bipolar outflow, SMA 2 is very likely a Class 0 source. SMA 1 has a bolometric temperature of 83 K and shows evidence for a higher temperature (350 K) component in its SED. This suggests a more evolved evolutionary state, consistent with a Class 0/Class I transition object. Its significantly higher luminosity ($17L_{\odot}$) also suggests that SMA 1 is a more massive protostar. When placed on a bolometric luminosity vs. temperature (BLT) diagram (Myers et al. 1998), SMA 2 is consistent with the evolutionary track of a $\leq 0.3\text{M}_{\odot}$ envelope when compared to the model tracks of Young & Evans (2005). SMA 1, with its slightly higher bolometric temperature, but far higher bolometric luminosity, is consistent with a $\sim 1 - 5\text{M}_{\odot}$ envelope mass. Caution must be used with the use of a BLT diagram to derive masses, since T_{bol} is not a good estimator of age, resulting in the rather wide range of acceptable masses for the two sources.

4.4. A young embedded low-mass cluster?

Schöier et al. (2006) believe that SMA 1 and SMA 2 form a protobinary system similar to IRAS 16293 (Walker et al. 1986). We do not find evidence that supports this conclusion. The two sources seem to be at different evolutionary states, with very different source properties. Our outflow data shows evidence for one large scale outflow associated with SMA 2, and at least one smaller outflow (associated with HH100-IR). A small outflow with an axis roughly orthogonal to the SMA 2 outflow could be driven by SMA 1. In addition, the “shell” of HCO^+ emission seems to be spatially centered on SMA 2, with little association with SMA 1. In the situation of a coeval protobinary, any shells of material would likely be surrounding the entire protobinary system, not a single member.

We postulate that the HCO^+ emission could be the result of the interaction of many molecular outflows, or could trace a shell of material around SMA 2, swept up by the outflow or by a lower velocity wind from a single object. Would such a shell be gravitationally bound to the central object, or would it be expanding? Using the mass estimate from the previous section, we can compare the kinetic energy of the possible shell to its gravitational potential energy. Here, we have maximized the mass estimate of the shell, and use the best estimates for the protostellar envelope mass and protostar mass derived from the BLT diagram. We calculate that the kinetic energy is more than a factor of 20 higher than the gravitational potential energy. This suggests that the material is not gravitationally bound to the central object. Further understanding of the kinematics and structure of the dense molecular gas in this region will require interferometric observations combined with zero spacing data from properly-sized single dish telescopes, a technique that is envisioned as a standard capability of the Atacama Large Millimeter Array (ALMA) (Wootten 2007). Similarly, mosaiced interferometric CO observations with zero spacing, or data from new, large single dish telescopes such as the Large Millimeter Telescope (LMT) should be able to more accurately trace the source(s) of the bipolar outflows.

5. Summary

We have observed the R CrA molecular cloud in the region surrounding the near-IR source IRS 7 with the Submillimeter Array in 1.1 mm continuum and the HCO^+ $J = 3 \rightarrow 2$ line. We present complementary SCUBA/JCMT 850 μm and 450 μm continuum images, Spitzer archival IRAC and MIPS 24 μm images and DesertStar/HHT ^{12}CO $J = 3 \rightarrow 2$ maps of the molecular outflow. We detect two compact continuum sources, SMA 1 and SMA 2 previously identified by Nutter et al. (2005) as SMM1B and SMM1C, which are not associated with any known near-IR counterparts but are detected at centimeter and hard

X-ray wavelengths. The brighter, spatially-extended source SMM1A is not detected in our interferometric observations. The SED of SMA 1 derived from the SMA, SCUBA and Spitzer data is best fit by a two component greybody with temperatures of 55 K and 344 K, and a long wavelength dust grain emissivity index $\beta = 1.3$. The bolometric temperature of the source is 83 K, with a bolometric luminosity of $17 \pm 6 L_{\odot}$. While SMA 2 is detected at 1.1 mm, 870 μm and 450 μm , we do not detect it at 24 μm or in any IRAC bands. From the flux density upper limit at 24 μm , we compute the maximum temperature greybody model consistent with the data to be 63 K with $\beta = 0.6$. The bolometric temperature is ≤ 70 K, and the bolometric luminosity is between 0.15 and 3.3 L_{\odot} . These results suggest that SMA 2 is a low mass ($\leq 0.3 M_{\odot}$) Class 0 source, while SMA 1 is a transitional Class 0/Class I object of higher envelope mass ($\sim 1\text{--}5 M_{\odot}$). We see evidence for a single large scale molecular outflow driven by SMA 2, with evidence for at least one more smaller outflow associated with HH-100IR (IRS1). The $\text{HCO}^+ J = 3 \rightarrow 2$ emission detected with the SMA is very clumpy in nature, with a complex velocity field consistent with a spherical shell of material blown by a wind from one or more of the members of the young cluster. This emission could also be explained by the interaction of outflows driven by the many YSOs in the region. Future interferometric observations with zero spacing and short baseline data will assist in determining the distribution of gas around these two protostars.

C.E.G. is supported by an NSF Astronomy and Astrophysics Postdoctoral Fellowship under award AST-0602290. We wish to thank Dr. Remy Indebetouw of the University of Virginia with his assistance in the PSF fitting photometry of the saturated MIPS 24 μm observations.

REFERENCES

- Andrews, S. M., & Williams, J. P. 2005, *ApJ*, 631, 1134A
- Boss, A. P., & Yorke, H. W. 1995, *ApJ*, 439, L55
- Brown, A. *ApJ*, 322, L31
- Caratti o Garatti, A., Giannini, T., Nisini, B., & Lorenzetti, D., 2006, *A&A*, 449, 1077
- Chen, W. P., & Graham, J. A. 1993, *ApJ*, 409, 319
- Chini, R., Kämpgen, K., Reipurth, B., Albrecht, M., Kreysa, E., Lemke, R., Nielbock, M., Reichertz, L.A., Sievers, A., & Zylka, R. 2003, *A&A*, 409, 235

- Choi, M. & Tatematsu, K. 2004, ApJ, 600, L55
- Cohen, M., Harvey, P. M., Wilking, B. A., & Schwartz, R. D., 1984, ApJ, 281, 250
- Davis, C. J., Smith, M. D., Eisloffel, J., & Davies, J. K., 1999, MNRAS, 308, 539
- Feigelson, E.D., Carkner, L., & Wilking, B.A. 1998, ApJ, 494, 215
- Forbrich, J., Preibisch, T., & Menten, K. M. 2006, A&A, 446, 155
- Forbrich, J., et al. 2007, A&A, 464, 1003
- Froebrich, D. 2005, ApJS, 156, 169
- Graham, J. A. 1993, PASP, 105, 561
- Groppi, C.E., Kulesa, C., Walker, C., & Martin, C.L. 2004, ApJ, 612, 946
- Groppi, C.E., Walker, C.K., Kulesa, C., Golish, D., Hedden, A., Narayanan, G., Lichtenberger, A.W., Kooi, J.W., Graf, U.U., Heyminck, S., 2004 Proc. SPIE, 5498, 290
- Hamaguchi, K., Corcoran, M.F., Petre, R., White, N.E., Stelzer, B., Nedachi, K., Kobayashi, N., & Tokunaga, A.T. 2005, ApJ, 623, 291
- Harju, J., Haikala, L.K., Mattila, K., Mauersberger, R., Booth, R.S., & North, H.L. 1993, A&A, 278, 569
- Hartigan, P., & Graham, J. A. 1997, AJ, 93, 913
- Henning, T., Launhardt, R., Steinacker, J., & Thamm, E. 1994, A&A, 291, 546
- Hildebrand, R.H. 1983, QJRAS, 24, 267
- Hogerheijde, M.R. *SFChem 2002* Eds. Charles L. Curry & Michel Fich. 2003, NRC Press, Ottawa, Canada, p. 44
- Holland, W.S., Robson, E.I., Gear, W.K., Cunningham, C., Lightfoot, J.F., Jenness, T., Ivison, R.J., Stevens, J.A., Ade, P.A.R., Griffin, M.J., Duncan, W.D., Murphy, A., & Naylor, D.A. 1999, MNRAS, 303, 659
- Jenness, T., & Lightfoot, J.F. 1999, Starlink User Note 216.6, Rutherford Appleton Laboratory, Particle Physics & Astronomy Research Council
- Knude, J., & Høg, E., 1998, A&A, 338, 897

- Koyama, K., Hamaguchi, K., Ueno, S., Kobayashi, N., & Feigelson, E. D. 1996, PASJ, 48, L87
- Levreault, R.M. 1988, ApJS, 67, 283
- Loren, R.B. 1979, ApJ, 227, 832
- Megeath, S.T., Allen, L.E., Gutermuth, R.A., Pipher, J.L., Myers, P.C., Calvet, N., Hartmann, L., Muzerolle, J., Fazio, G.G. 2004, ApJS, 154, 367
- Myers, P.C., & Ladd, E.F., 1993, ApJ, 413, L47
- Myers, P.C., Adams, F.C., Chen, H., & Schaff, E. 1998, ApJ, 492, 703
- Nutter, D.J., Ward-Thompson, D., & Andre, P. 2005, MNRAS, 357, 975
- Reynolds, S. P. 1986, ApJ, 304, 713
- Sandell, G., Jessop, N., & Jenness, T. 2001, "The SCUBA map reduction Cookbook", Starlink Cookbook 11.2, Rutherford Appleton Laboratory, Particle Physics & Astronomy Research Council
- Sault, R.J., Teuben, P.J., & Wright, M.C.H., 1995, in ASP Conf. Ser. 77: Astronomical Data Analysis Software and Systems IV, Eds. R.A. Shaw, H.E. Payne, & J.J.E. Hayes (Astronomical Society of the Pacific: San Francisco), p. 433
- Schöier, F.L., Jørgensen, J.K., Pontoppidan, K.M., & Lundgren, A.A. 2006, A&A, 454, L67
- Snell, R.L., Scoville, N.Z., Sanders, D.B., & Erickson, N.R. 1984, ApJ, 284, 176
- Strom, S.E., Grasdalen, G.L. & Strom K.M., 1974, ApJ, 191, 111
- Taylor, K.N.R., & Storey, J.W.V. 1984, MNRAS, 209, 5
- van den Ancker, M., 1999, Ph.D. Thesis, University of Amsterdam
- Walker, C.K., Lada, C.J., Young, E.T., Maloney, P.R., & Wilking, B.A. 1986, ApJ, 309, L47
- Wang, H., Mundt, R., Henning, T., Apai, D. 2004, ApJ, 617, 1191
- Wilking, B. A., McCaughrean, M. J., Burton, M. G., Giblin, T., Rayner, J. T., & Zinnecker, H. 1997, AJ, 114, 2029
- Wilking, B. A., Taylor, K. N. R., & Storey, J. W. V. 1986, AJ, 92, 103

Wootten, A. 2007, ArXiv Astrophysics e-prints, arXiv:astro-ph/0702668

Young, C.H. & Evans, N.J. 2005, ApJ, 627, 293

Zhao, J-H. 2006, “Miriad User’s Guide to the Reduction of SMA Data”

Table 1. SMA 271 GHz continuum sources

Source	$\alpha(2000.0)$ [^h ^m ^s]	$\delta(2000.0)$ [[°] ' " []]	$\theta_a \times \theta_b$ [" \times "]	P.A. [[°]]	$d_a \times d_b$ [AU \times AU]	S(1.1 mm) ^a [mJy]
SMA 1	19 01 56.416	−36 57 27.85	1.1×0.5	52	220×140	300 ± 17
SMA 2	19 01 55.289	−36 57 17.03	<1	...	<170	280 ± 17

^aThe quoted uncertainty does not include the 20% uncertainty in the overall flux scale.

Table 2. Positions, deconvolved sizes and integrated flux densities of SCUBA sources in the R Cr A cloud core following naming convention in (Nutter et al. 2005)

Sub-mm source	$\alpha(2000.0)$ [^h ^m ^s]	$\delta(2000.0)$ [[°] ['] ^{''}]	$\theta_a \times \theta_b$ [^{''} \times ^{''}]	P.A. [[°]]	S(850 μ m) [Jy]	S(450 μ m) [Jy]	Other Designations
SMM 1 A ^a	19 01 55.23	−36 57 46.0	43 \times 27	−80	14.5 \pm 2.2	151 \pm 30	vdA 2&4
SMM 1A S	19 05 54.97	−36 58 29.0	14 \times 13	...	1.2 \pm 0.2	6.9 \pm 1.7	
SMM 1B ^b	19 01 56.35	−36 57 28.1	3.1 \times 1.3	...	1.5 \pm 0.2	5.2 \pm 0.5	vdA 5, SMA 1, I 4, B 10E, X _E
SMM 1C	19 01 55.29	−36 57 17.5	3 \times <1	−9	1.1 \pm 0.2	2.4 \pm 0.7	vdA 3, SMA 2, B 9, FCW 6, CT 2&3
SMM 2	19 01 58.57	−36 57 09.4	7 \times 6	...	1.2 \pm 0.2	5.8 \pm 1.5	vdA 6, I 3, WMB 55
SMM 3 ^c	19 01 50.81	−36 58 11.3	9 \times 7	...	1.5 \pm 0.2	>5.4 \pm 1.0	vdA 1, IRSi, HH 100-IR, I 7, B 8, FCW 4, K 6
SMM 4	19 01 47.97	−36 57 17.6	40 \times 29	−4	4.8 \pm 0.7	...	IRS 5, I 10, I 9

^aResolved into two cores at high angular resolution, see e.g. Fig. 2 and van den Ancker (1999)

^bAppears extended at 450 μ m consistent with SMA results, but the errors from the Gaussian fits are large

^cAt the edge of the 450 μ m map; Coordinates & size taken from 850 μ m, flux density at 450 μ m is underestimated.

Note. — The prefixes used for the source numbers in column 'Other Designations' come from: vdA (van den Ancker 1999), SMA (Table 1), I (IRAC sources, Table 3), B (Brown 1987), FCW (Feigelson et al. 1998), CT (Choi & Tatematsu 2004), WMB (Wilking et al. 1997), K (Koyama et al. 1996), X (Hamaguchi et al. 2005)

Table 3. Positions and flux densities of IRAC 8 μm sources in the R CrA cloud core.
Photometric uncertainties are $\sim 10\%$.

nr	Optical/near-IR counterpart	$\alpha(2000.0)$ [h m s]	$\delta(2000.0)$ [$^{\circ}$ ' "]	S(3.6 μm) [mJy]	S(4.5 μm) [mJy]	S(5.8 μm) [mJy]	S(8 μm) [mJy]	comment
1	T CrA	19 01 58.77	−36 57 50.0	...	2636.1	2772.3	3113.8	saturated at 3.6 μm
2	IRS 4	19 01 58.64	−36 56 17.1	77.9	55.3	45.9	22.2	
3	WMB 55	19 01 58.54	−36 57 08.7	26.7	71.0	143.2	189.2	
4		19 01 56.39	−36 57 28.2	41.9	251.1	687.3	1034.2	
5 ^a	IRS 7	19 01 55.32	−36 57 22.1	58.2	245.5	666.4	1099.3	
6	R CrA ^b	19 01 53.65	−36 57 07.3	saturated
7	IRS 1, HH 100-IR	19 01 50.68	−36 58 09.7	4024.6	6247.0	13490.8	...	saturated at 8 μm
8	IRS 6	19 01 50.50	−36 56 38.1	123.3	170.4	213.0	215.5	
9	IRS 5N	19 01 48.46	−36 57 14.8	15.9	36.0	56.4	93.9	
10	IRS 5	19 01 48.02	−36 57 22.3	435.5	835.4	1294.0	1973.8	

^aPhotometry more uncertain, because the source emission is affected by one of the diffraction spikes from R CrA

^bPosition from 3.6 μm , one saturated pixel; optical position (Simbad): RA = 19^h 01^m 53^s.65, Dec = −36 $^{\circ}$ 57' 07".6

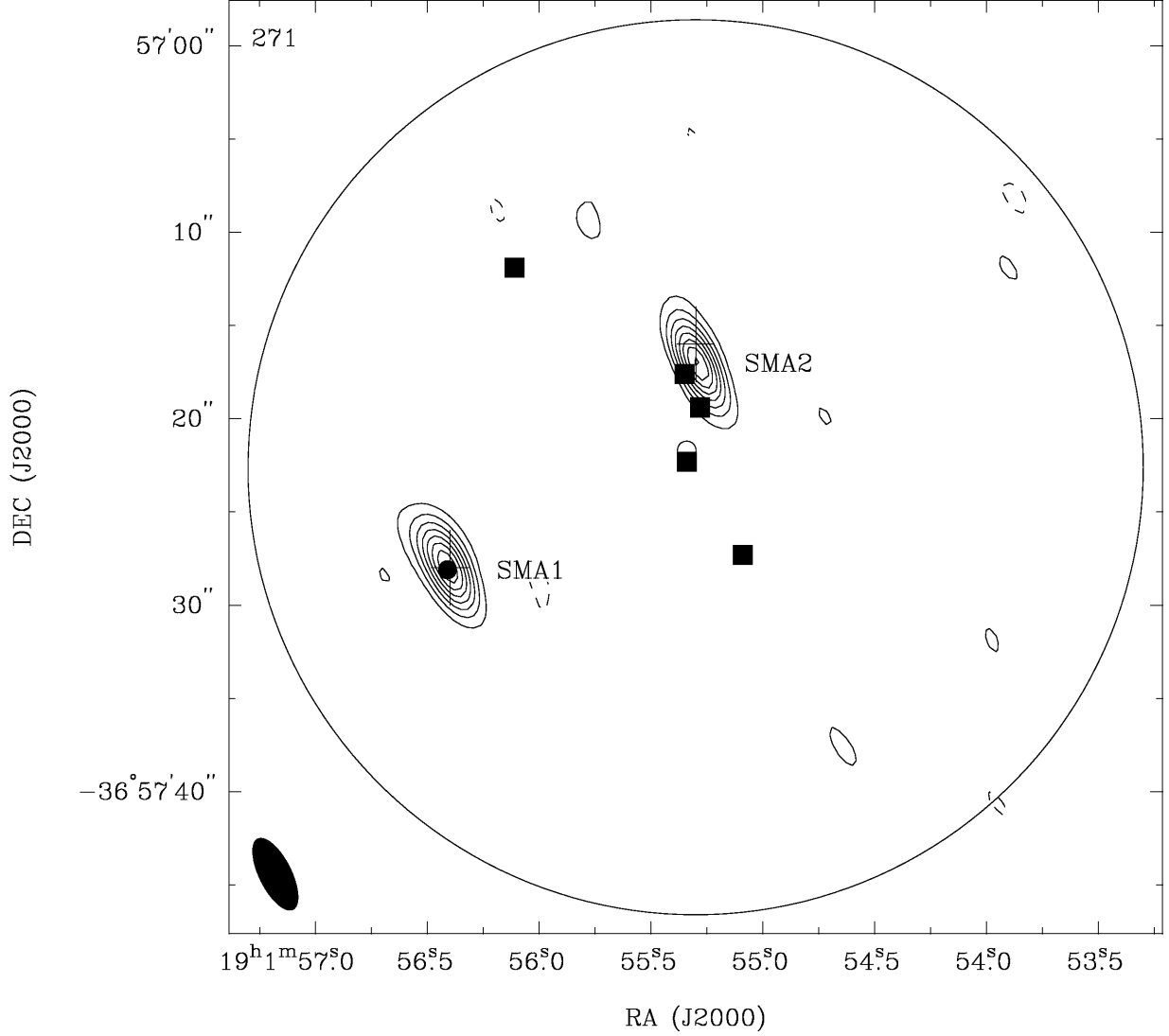


Fig. 1.— SMA continuum interferometric image at 271 GHz. Two sources are detected of approximately equal flux density (0.3 Jy and 0.28 Jy). Crosses mark the positions of centimeter detections from Feigelson et al. (1998). The open circle marks the position of IRS7, while the boxes mark the 7 mm sources from Choi & Tatematsu (2004). The filled circle marks the location of the IRAC IR source associated with SMA 1. Contours are spaced at 4σ , with the lowest contour at 4σ (36 mJy).

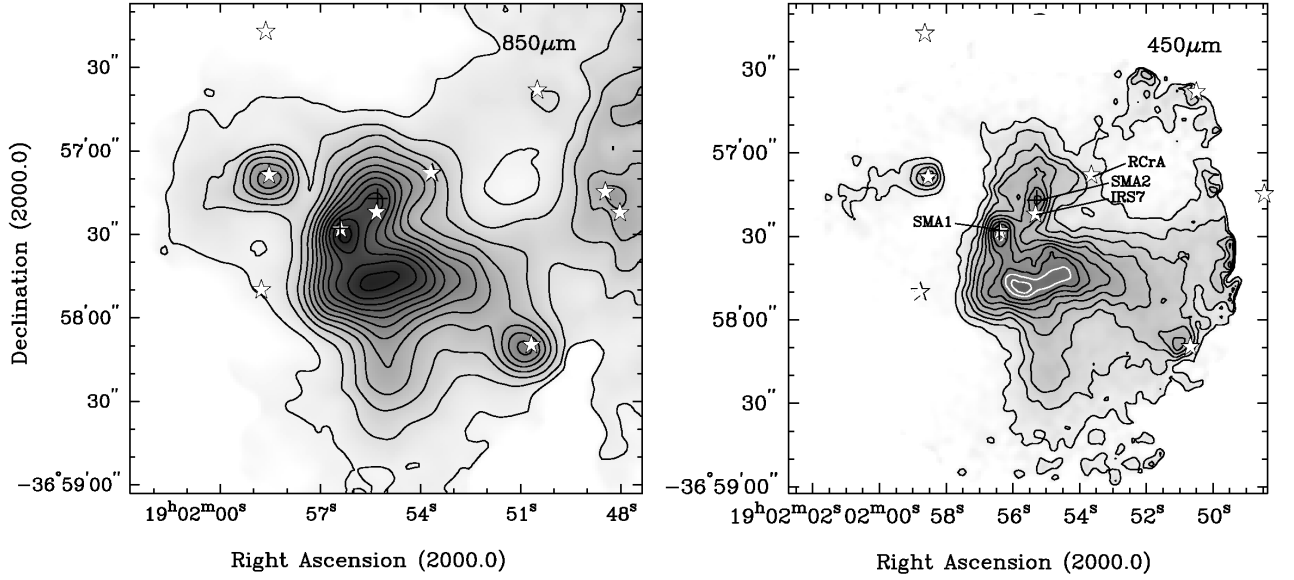


Fig. 2.— 850 μm (Left) and 450 μm (Right) SCUBA maps of the R CrA cloud core. Star symbols mark the positions of IRAC 8 μm sources and the crosses show the two SMA sources. These two sources as well as IRS 7 and the HAEBE star R CrA are labeled on the 450 μm image. Only the 450 μm data clearly resolves SMA 1 and SMA 2. The minimum contour for the 850 μm image is 0.15 Jy, with contours separated by 0.2 Jy. For the 450 μm image, the first two contours are 1.4 and 2.5 Jy, with other contours spaced by 0.9 Jy.

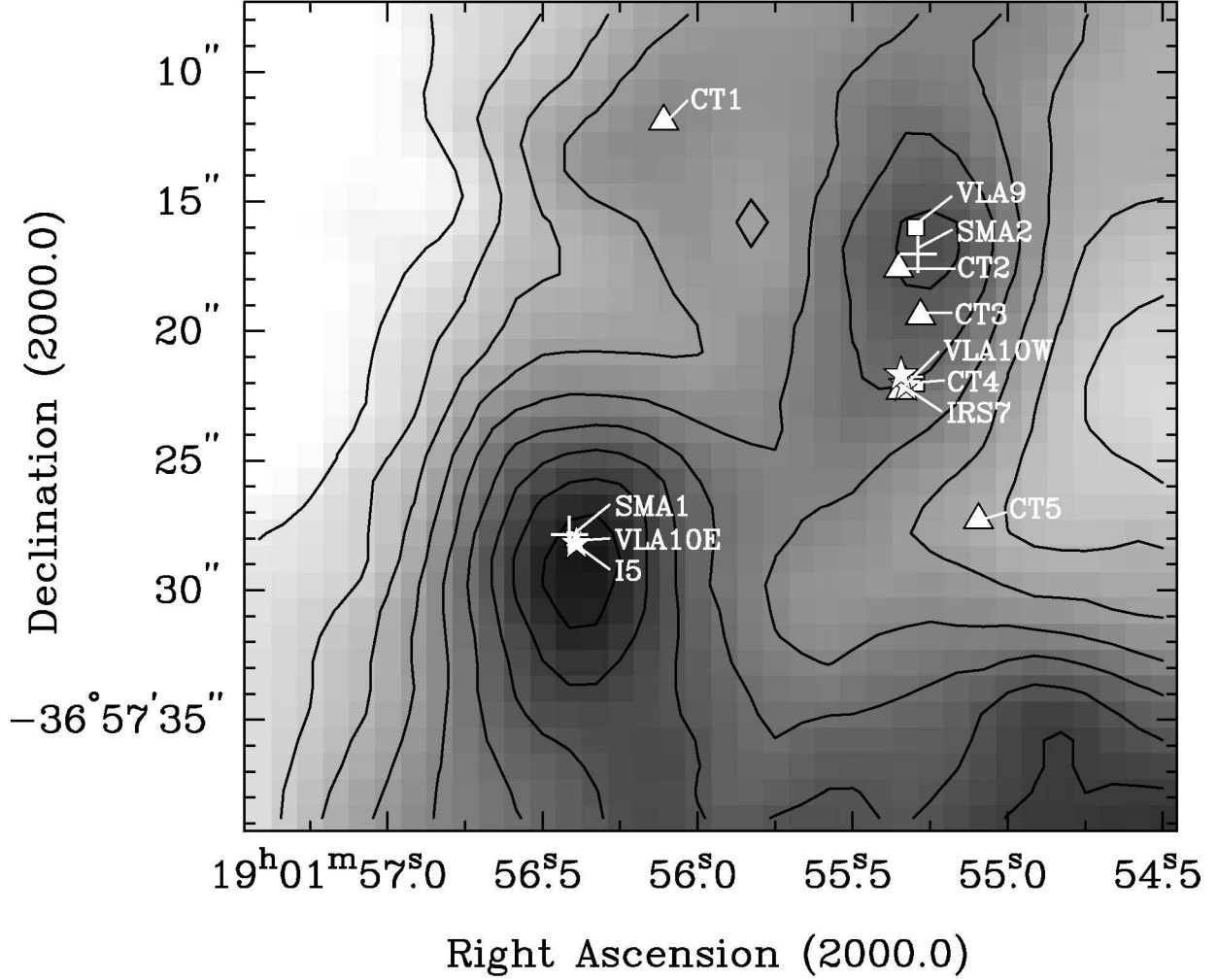


Fig. 3.— Blow-up of the SCUBA 450 μm continuum map (grayscale and contours) showing SMA 1, IRS 7 and SMA 2. Crosses mark the SMA positions, stars the IRAC positions, filled squares the centimeter VLA positions (Feigelson et al. 1998), filled triangles the 7 mm VLA positions (Choi & Tatematsu 2004). The first two contours are 1.4 and 2.5 Jy, with other contours spaced by 0.9 Jy.

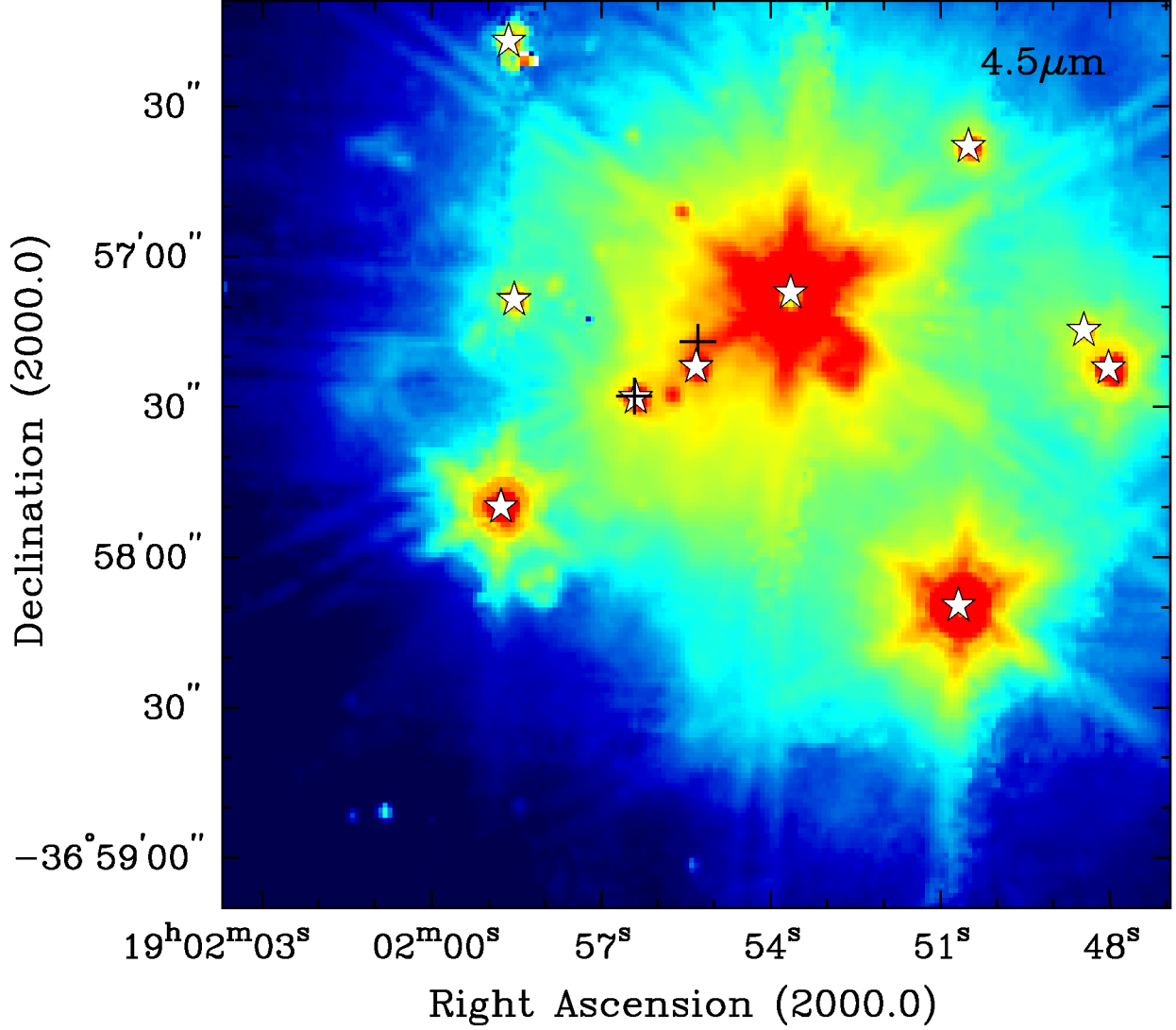


Fig. 4.— IRAC 4.5 μm image of the R CrA region corresponding to figure 2. This image is a composite of both long and short exposure time data to improve dynamic range. A logarithmic stretch has been applied to emphasize fainter features. Sources are plotted identically to figure 2.

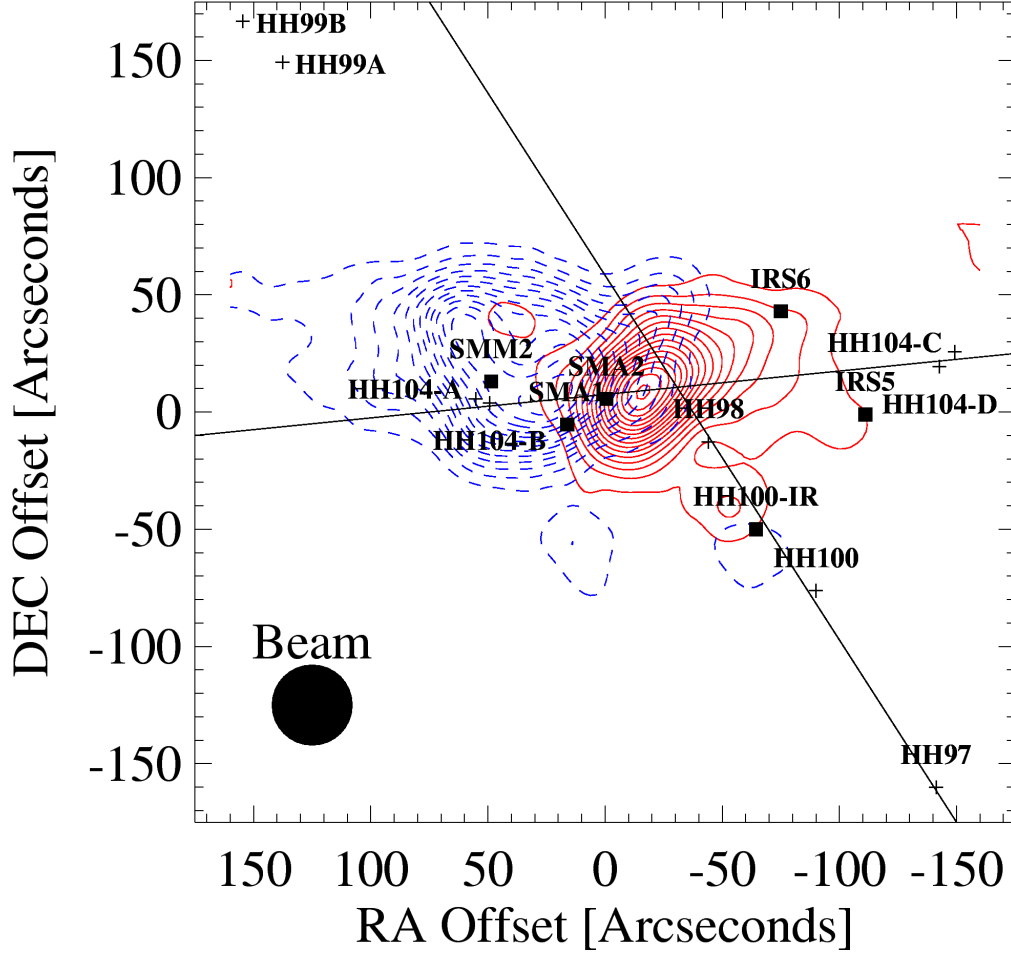


Fig. 5.— $^{12}\text{CO } J = 3 \rightarrow 2$ outflow map of R CrA. The map covers an area of $5' \times 5'$. The blue-shifted emission is integrated over the velocity interval -10 to 3 km s^{-1} , while the red interval is 10 to 21 km s^{-1} . Contours are separated by two sigma, with the lowest contour at two sigma, calculated from the noise in the spectra off the line integrated over the same velocity width. Optically detected Herbig-Haro objects are marked with plus symbols, while IR and sub-mm sources are marked with squares. Lines connect HH objects we believe are related to molecular outflow lobes.

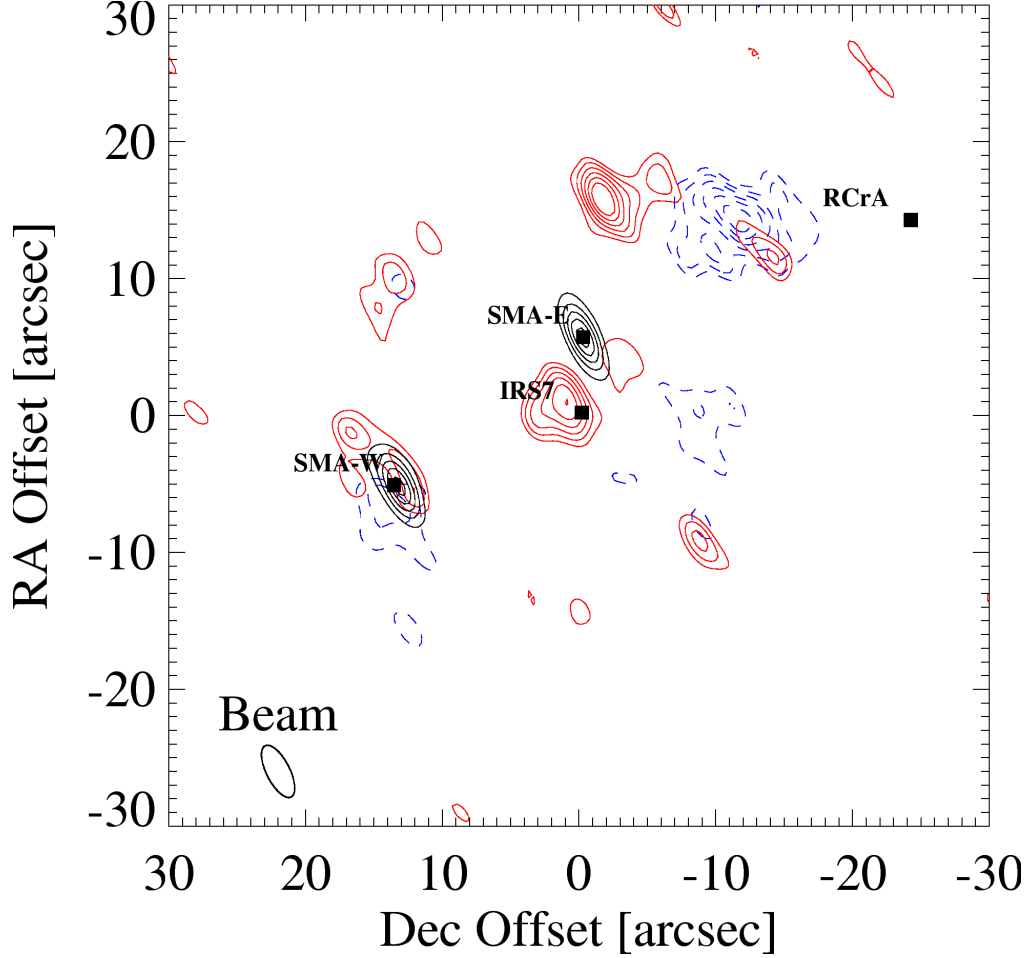


Fig. 6.— HCO^+ $J = 3 \rightarrow 2$ emission overlaid on the 271 GHz continuum contours (solid black). Red solid lines are integrated from 5.7 to 9.3 km s^{-1} , and the dashed blue lines are integrated from 3.8 to 5.7 km s^{-1} . Contours are separated by 1σ , with the lowest contour at 1σ . The HCO^+ clumps seem to be distributed roughly spherically around SMA 2, and show no direct association with the continuum sources nor with the large scale CO outflows shown in Figure 5.

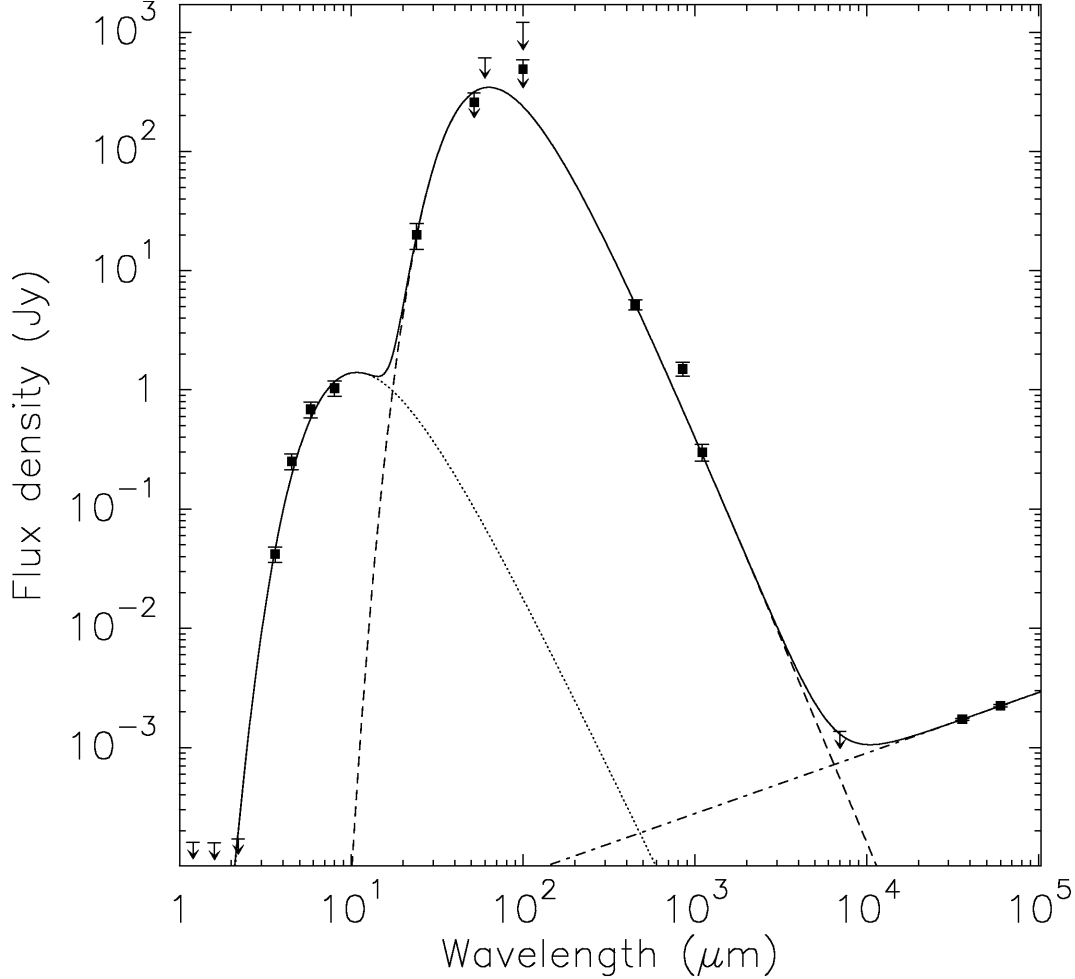


Fig. 7.— Spectral energy distribution of the source SMA 1. 24 μm MIPS and IRAC data points are derived from Spitzer archival data, while the 1.1 mm, 850 μm and 450 μm data are from this work. The 850 μm measurement is likely influenced by emission from SMA 2 which is only barely resolved from SMA 1 in the single-dish data. The 4σ upper limit at 7 mm is from Choi & Tatematsu (2004). The data are fit with a two temperature diluted blackbody plus a power-law free-free component. The upper limits at 60 and 100 μm are from the PSC detection of IRAS 18585-3701. They are drawn as upper limits because SMA 1 and SMA 2 are unresolved in these data. Likewise, the detections at 52 and 100 μm are from the Kuiper Airborne Observatory with a 38'' to 47'' beam (Cohen et al. 1984). The spectral index of the free-free component plotted is $F_\nu \sim \nu^{-0.5}$, as determined by the two measurements at centimeter wavelengths (6 cm by Brown (1987) and 3.6 cm by Forbrich et al. (2007)).

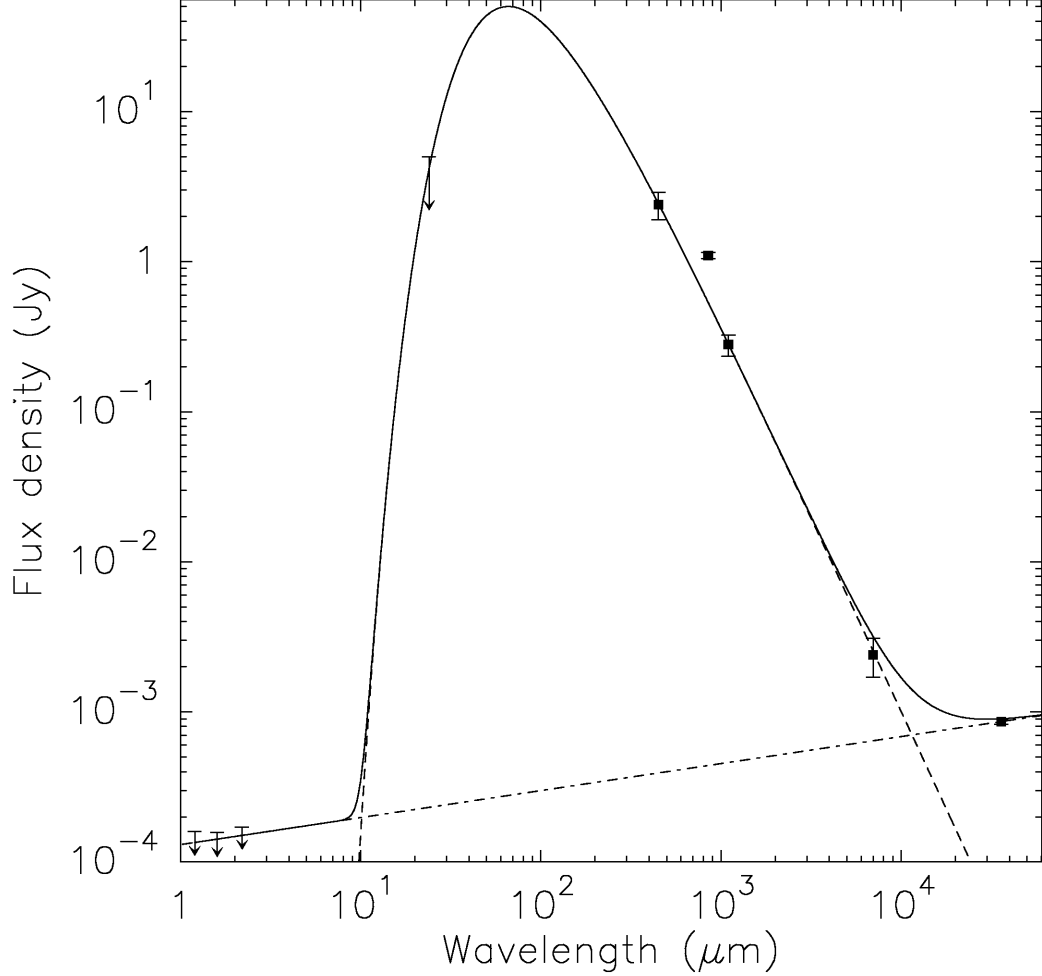


Fig. 8.— Spectral energy distribution of the source SMA 2. The 850 μm measurement is likely influenced by emission from SMA 1 which is only barely resolved from SMA 2 in the single-dish data. The detection at 7 mm is from source 2 of Choi & Tatematsu (2004). The flux density at 3.6 cm is the average of ten measurements from Forbrich et al. (2006) and Feigelson et al. (1998). The data are fit with a power-law free-free component ($F\nu \propto \nu^{-0.1}$) plus a single temperature greybody, using the 24 μm upper limit to find the maximum temperature diluted blackbody consistent with the data. The spectral index of the free-free component plotted is $F_\nu \sim \nu^{-0.18}$, the shallowest value consistent with all the data.